Journal of Minerals and Materials Characterization and Engineering, 2024, 12, 100-111
https://www.scirp.org/journal/jmmce
ISSN Online: 2327-4085
ISSN Print: 2327-4077

# Metallurgical Microstructure Complexity in the Electron Beam Welding (EBW) Joint of Ti6246

**Daniel Moreno*, Yohanan Nachmana, Roei Saraga, Tal Rokah, Denis Panchenco, Michael Mansano, Elinor Itzhaky, Moshe Shapira**

Beth Shemesh Engines LTD, FAA & EASA, Beth Shemesh, Israel
Email: *danielm@bsel.co.il

**How to cite this paper:** Moreno, D., Nachmana, Y., Saraga, R., Rokah, T., Panchenco, D., Mansano, M., Itzhaky, E. and Shapira, M. (2024) Metallurgical Microstructure Complexity in the Electron Beam Welding (EBW) Joint of Ti6246. *Journal of Minerals and Materials Characterization and Engineering*, **12**, 100-111.
https://doi.org/10.4236/jmmce.2024.122008

**Received:** February 5, 2024
**Accepted:** March 26, 2024
**Published:** March 29, 2024



## Abstract

Electron Beam Welding (EBW) is employed to both melt and unite materials, influencing their thermal history and subsequently determining the microstructure and properties of the welded joint. Welding Titanium alloys involves undergoing local melting and rapid solidification, subjecting the material to thermal stresses induced by a thermal expansion coefficient of 9.5 × 10 m/m˚C. This process, reaching range temperatures from the full melting alloy to room temperature, results in phase formation dictated by the thermodynamic preferences of the alloyed elements, posing a significant challenge. Recent efforts in simulation and calculations have been undertaken elsewhere to address this challenge. This study focuses on a joint of two plates with differing cross-sectional areas, influencing heat transfer during welding. This report presents a case study focusing on the metallurgical changes observed in the microstructure within the welded zone, emphasizing alterations in the cooling rate of the welded joint. The investigation utilizes optical metallography, Vickers's Hardness testing, and SEM (scanning electron microscopy) to comprehensively characterize the observed changes in addition to heat transfer simulation of the welded zone.

## Keywords

Ti Alloys, Welding, Phase Formation, Hardness, Metallography

## 1. Introduction

Titanium alloys are highly valued in aerospace applications due to their exceptional combination of strength, low density, and corrosion resistance. Here are some key reasons why titanium alloys are extensively used in aerospace: High Strength-to-Weight Ratio (HSWR) property as a crucial to aerospace engineering, where minimizing weight while maintaining structural integrity is a primary concern due to fuel efficiency; Corrosion Resistance (CR) essential to varying atmospheric conditions in aero-engines and space shuttle; High Temperature Performance (HTP) around 425˚C, Low Thermal Expansion (LTE) crucial for dimensional stability and in components and Fatigue Resistance (FR) essential to cyclic loading and long-term reliability [1]. Ti-6-4, Ti-6-2-4-6, and Ti-17, are effective up to 300˚C, are utilized in the fan and low-pressure compressor sections of modern high-bypass-ratio aircraft engines. As mentioned early, the specific strength (density-corrected strength) of these titanium alloys is crucial for achieving the increased bypass ratios seen in contemporary, quieter, and more fuel-efficient engines. Near-$\alpha$ alloys like Ti-6-2-4-2S and IMI 834 are employed in the front of the high-pressure compressor. Also, Ti-6-2-4-2S operates up to 500˚C, while IMI 834 can withstand up to 600˚C. These alloys are approximately 50% lighter than the steel or Ni-base alloys they replaced in earlier jet engines, contributing to weight savings [2].

The integration of computer simulations, particularly through finite element modelling, has significantly contributed to the understanding and optimization of manufacturing processes like EBW and IFW for titanium alloy components in the aerospace industry. This knowledge is crucial for meeting the increasing demands and harsh working conditions imposed on modern aerospace components [3].

Electron Beam Welding (EBW) used to melt and join materials change thermal history and in determining the microstructure and properties of the welded joint. The rapid heating and cooling rates associated with EBW can influence on the formation of phases, grain, and metallurgical structure on the welded region [4] [5]. The microstructure of titanium alloys is closely tied to their mechanical properties. Rapid cooling rates in welding processes can lead to the formation of fine-grained structures, affecting strength and toughness. In EBW, the heat-affected zone (HAZ) adjacent to the weld and the fusion zone itself undergo distinct changes in microstructure [6]. Controlling the cooling rate can influence the size and distribution of phases. Joining of titanium alloys using processes like EBW requires a deep understanding of material compatibility and the potential formation of intermetallic compounds at the joint interfaces [7]. The practical considerations and challenges associated with moving heat sources in a thermal process, particularly in welding are very important to achieve understanding of the metallurgical structures in the affected zone. The complexity of the calculations involved in estimating thermal features in welding was approached by Mendez [8]. In the present work asymmetric joint configuration of two, practically, infinites plates of Ti6246 were Electron Beam Welded to observe the effect of the heat transfer during cooling process due to the asymmetric. Basic heat transfer calculation was carried out and related to the metallurgical structure. Optical metallography and micro-hardness are reported.

## 2. Experimental

The Titanium $\alpha + \beta$ phase alloy utilized in this study is Ti-6-2-4-6, and its nominal chemical composition is detailed in **Table 1**. The alloy underwent heat treatment following AMS 4981 standards, involving solution treatment and aging at 885˚C for 1 hour, followed by 705˚C for 1 hour, both in an air-cooled environment. Although Mechanical Properties were assessed, they are not included in this presentation. The recorded values are as follows: 970 MPa for 0.2% Yield Stress, 1056 MPa for Ultimate Tensile Strength (UTS), and 24% deformation.

The schematic representation of the plate edges subjected to the welding process is depicted in **Figure 1(a)** & **Figure 1(b)**. Using a commercial device, two electron beam welds (EBW) were performed on the same joint. The first run utilized 136 kV and 10 milliamperes for a two-millimeter spot diameter, while the second run used 136 kV and 11 milliamperes, maintaining the two-millimeter spot diameter. Both runs covered a length of 100 mm at a welding speed of 50 cm/min. The high-speed electrons, diverging from the source, were focused to a 1 - 3 mm spot size to achieve the required power density.

For metallurgical and hardness inspections, a cross-section of the weld joint was cut and observed and characterized by optical and SEM metallography in addition of Vicker's hardness test of the different zones. Simulation of the heat transfer and the heat flow in the welded zones was carried out at different times after the welding and presented.

## 3. Results

**Figures 1(a)-(e)** shows the different zones of the EBW cross sections and present the changing of the metallurgical structure that was obtained during the process. **Figure 1(a)** present the sketch of the jointed parts before the welding. In **Figure 1(b)** the jointed parts are presented before etching and the numbers of interested zones that have been observed and investigated. **Figure 1(c)** shows the etched cross section with a Kroll solution which does not expose the metallurgical structure of the fused zone in the weld. After few tasks with different solution and electrolytic polishing techniques, the fused zone exposed the microstructure by 10% HF 20% $HNO_3$ 70% $H_2O$ etching as shown in **Figure 1(d)**. **Figure 1(e)** is a kind of photoshop of **Figure 1(c)** and **Figure 1(d)** to present the microstructures of the basic metal and the fused zone together. The heat effected zone (HAZ) is more difficult to expose from the microstructure point of view but was exposed in a different metallography in **Figure 2(b)**. **Figures 2(a)-(d)**

**Table 1.** Nominal alloy composition (weigh pct).

| Element / Alloy | Al | Sn | Zr | Mo | Fe | Ti | traces |
|---|---|---|---|---|---|---|---|
| Ti 6246 $\alpha + \beta$ phases alloy | 5.50 - 6.50 | 1.75 - 2.25 | 3.50 - 4.50 | 5.50 - 6.50 | <0.15 | Bal. | Less than 0.04, 0.15, 0.0125, 0.005 and 0.04, C, O, H, Y and N, respectively |

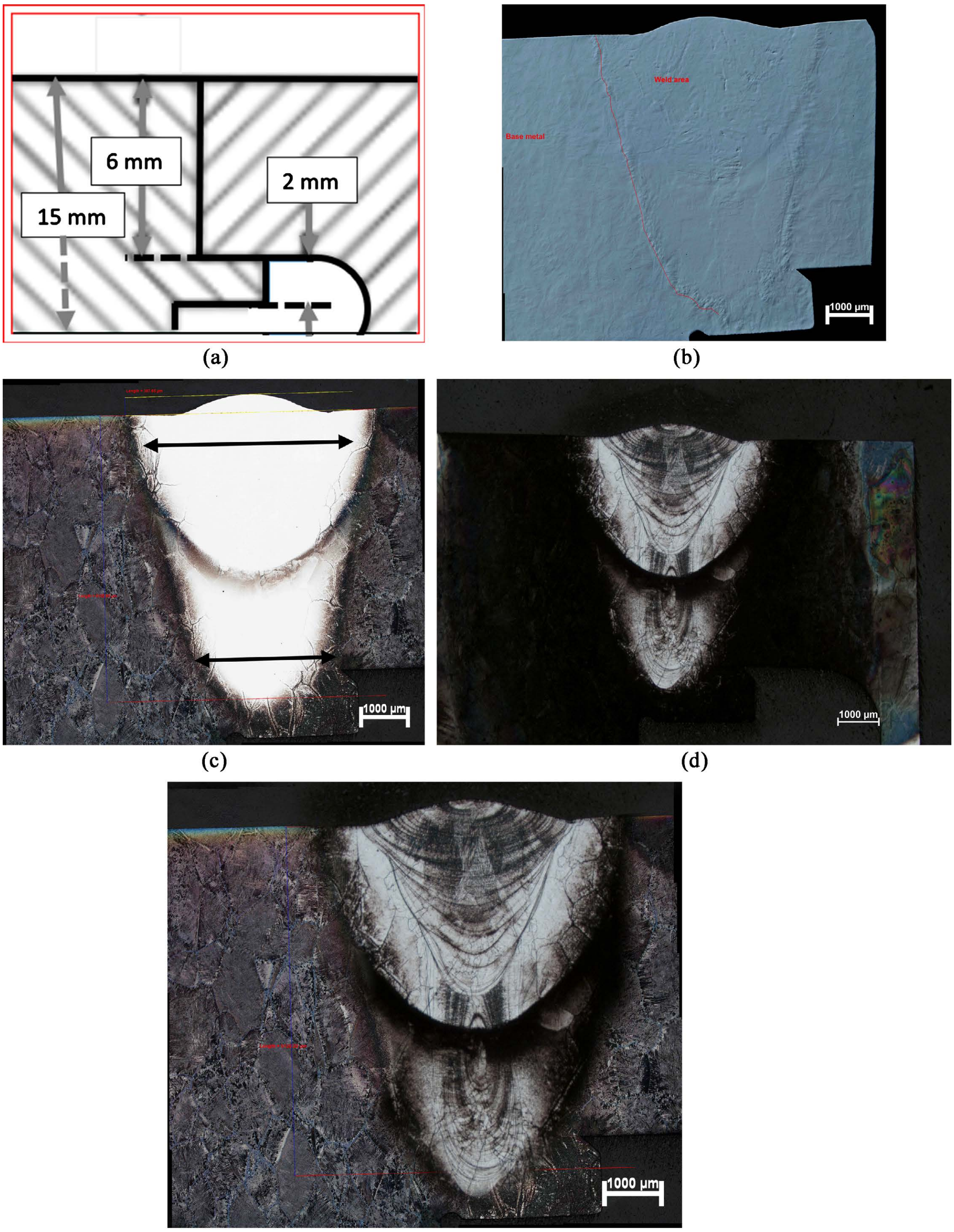


**Figure 1.** Cross section of the welded Ti-6-2-4-6, (a) Welded zone draft before EBW, (b) Welded zone after EBW, (c) Welded zone after the EBW and etched with a Kroll's reagent, The arrows are the path of the Vickers Hardness that are shown in Figure 4 and Figure 5. (d) Welded zone after the EBW and 10% HF 20% $HNO_3$ 70% $H_2O$ etched, (e) Superposition of (c) and (d). Two runs of welding; first run in the bottom and second run on the top.

show the 4 areas 1 to 4 marked in Figure 1(b). Figure 2(a) shows the equiaxed grain microstructure of the as received alloy Ti-6-2-4-6 with a very fine acicular $\alpha'$ phase that grow close perpendicular to the grain boundaries in small amount

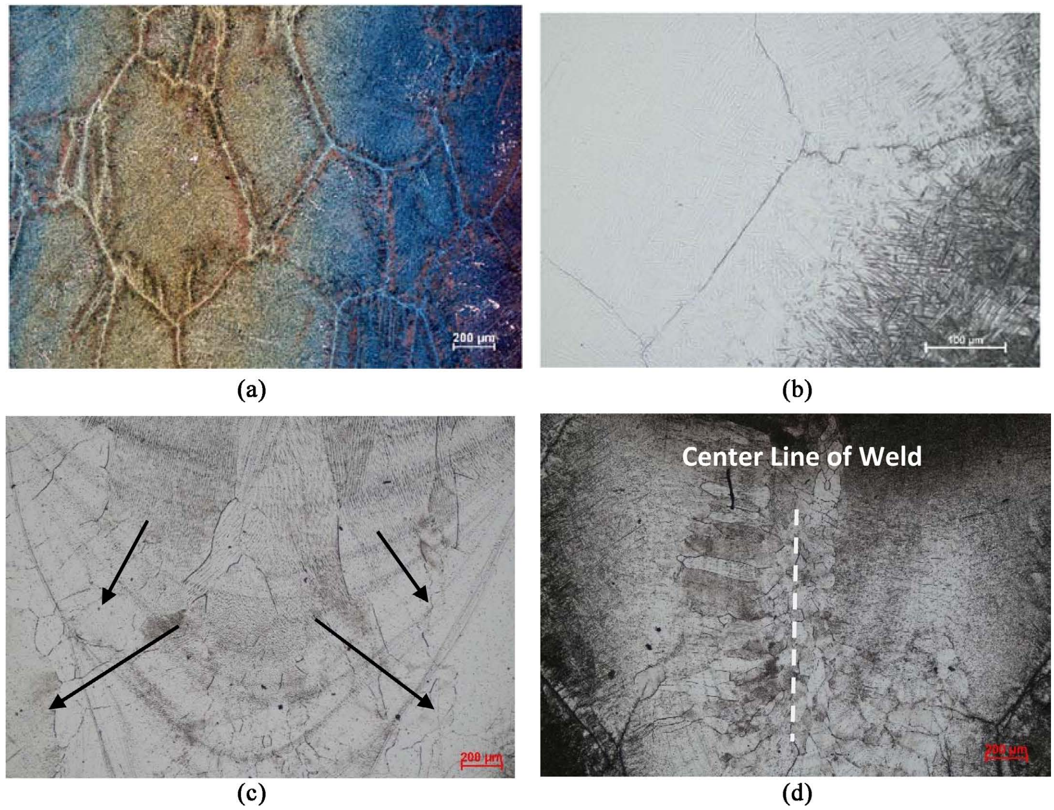


**Figure 2.** Cross sections of the welded Ti-6-2-4-6 in different zones when a, c and d at same magnification; (a) Bulk of the homogenized and aged received base metal, (b) HAZ zone as presented in Figure 1(b) by no. 1, (c) Second run of the fused zone after the EBW, as presented in Figure 1(b) by no. 2, and (d) First run of the fused zone after EBW, as presented in Figure 1(b) by no. 3.

transformed from the prior $\beta$ phase. The difference between $\alpha$ and $\alpha'$ is the saturation level when $\alpha$ is saturated and $\alpha'$ is pre-saturated in the $\beta$ phase. Figure 2(b) shows the effect of the additional heat due to the welding process on the basic metal where the structure emphasis a martensite $\alpha'$ phase by very fine serrated $\alpha'$. Figure 2(c) and Figure 3(b) show the second welding run after the full joining of the 2 parts of the Ti-6-2-4-6 basic plates and the heat transfer to the edges was improved due to the continuity of the metal after the first weld. The picture in Figure 2(c) shown a very fine lamellar $\alpha'$ formation attributed to thermal stresses and a good heat transfer from the welding zone. Also, the solidification front lines can be observed with a parabolic form and the assumed perpendicular direction of the heat transfer presented by arrows in some of the solidification lines. Larges arrows present the first zone to be solidified where equiaxed grains can be observed. In the smallest arrows zone, the last zone to be salified, the finest lamellar $\alpha'$ structure can be observed with lager grains with some preferred orientation. Enhanced metallography of this zone can be observed in Figure 3(b). Figure 2(d) is from the first welding run in the bottom of the (zone 4 in Figure 1(d)) where the difference in the microstructure is attributed to the different heat transfer rate between two sides of the center line welding. Preferred grow orientation is observed in the left side when the right-side

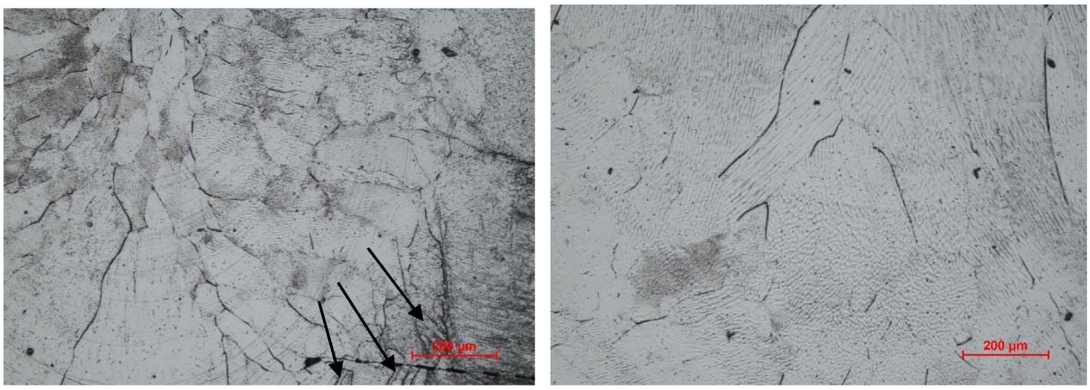


(a) (b)

**Figure 3.** Enhanced cross sections of the welded Ti-6246 in the fused zones; (a) First run of the fused zone after EBW, (b) Second run of the fused zone after the EBW.

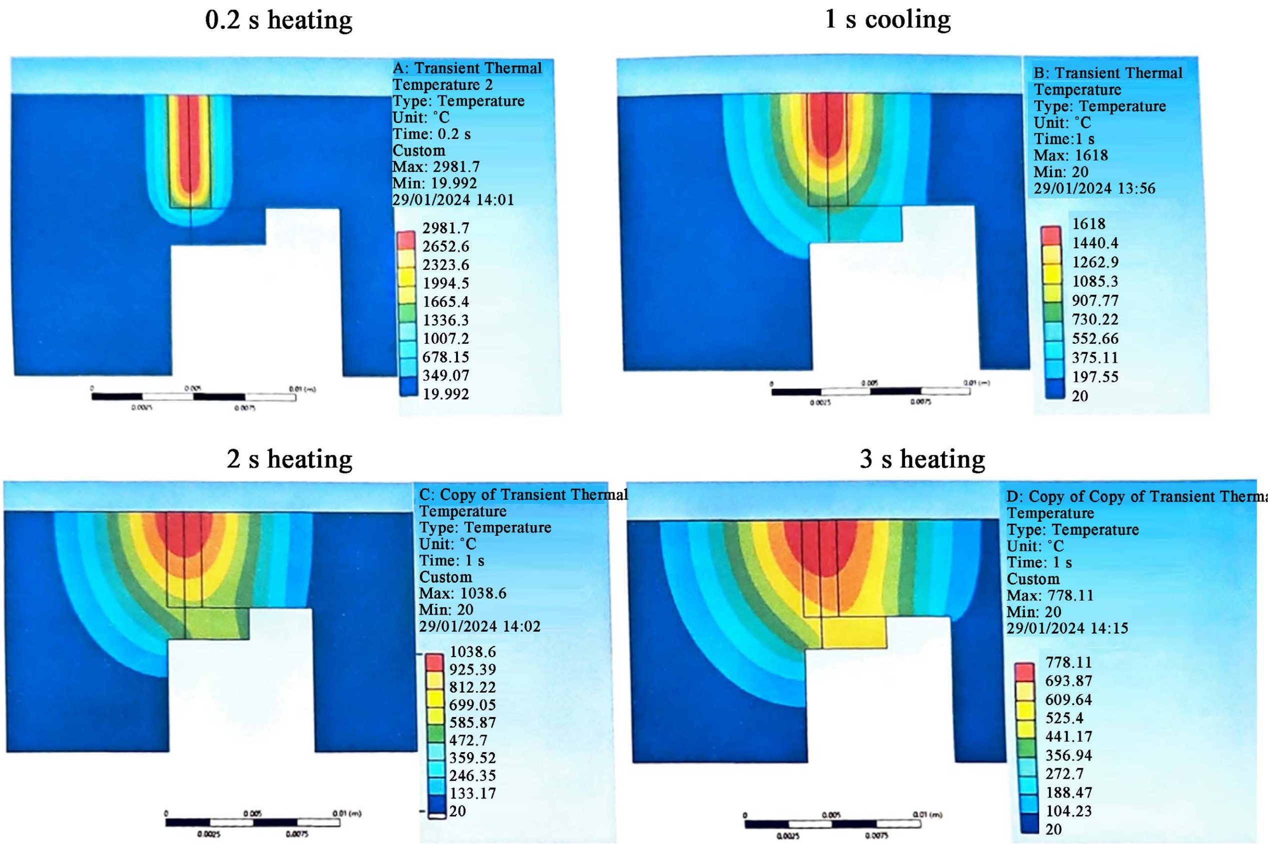


**Figure 4.** Simulation was carried out at 0.2, 1, 2 and 3 seconds after the weld process according to the sketch in **Figure 1(a)**.

present equiaxed grains, both with the same microstructures structure inside the grains. **Figure 4** shows the simulation of the heat transfer and the heat flow according to the temperature changes during the first 3 seconds after the melting, according to **Figure 1(a)** configuration used for the calculation. Coarsening of acicular $\alpha'$ and primary $\alpha''$ (probably orthorhombic phase mention latter) grain can be observed and marked by the arrows in **Figure 3(a)** close to the carbide's traces zone reported elsewhere as $Ti_2AlC$ as a stochiometric possibility [9]. **Figure 5** show the

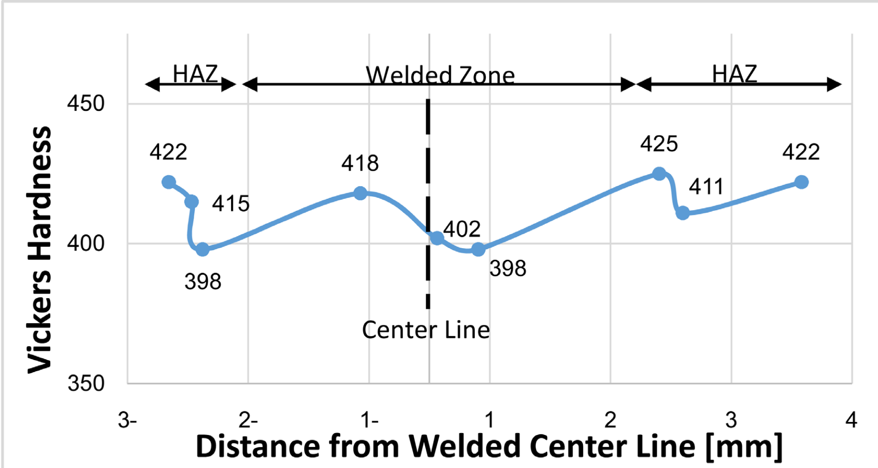


**Figure 5.** Vickers Hardness in the Fused Zone of the Second EBW Run and the respective distance from the center line of the welded zone in a plot and in **Table 2** carried out along the upper line and arrows shown in **Figure 1(c)**.

**Table 2.** Vickers hardness in the fused zone of the second EBW run.

| Zone | Vickers Hardness | Distance from Center Line [μm] |
|---|---|---|
| Left HAZ | 422 | −2158.45 |
| | 415 | −1969.66 |
| | 398 | −1878.36 |
| Fused Metal | 418 | −571.60 |
| | 402 | 64.23 |
| | 398 | 404.44 |
| Right HAZ | 425 | 1903.86 |
| | 411 | 2098.73 |
| | 422 | 3081.56 |

Vickers Hardness values obtained along the path shown in **Figure 2(c)** in the upper side of the welded zone performed in the second run. No majors' changes can be observed between the welded zone and the HAZ. **Table 2** summarizes the values and the distances from the center line of the welded parts. Similarly, in **Figure 5** for the bottom of the welded zone carried out in the first run of the EBW, and 3 additional indentation that were carried out in the basic metal. There is an enhancement of the hardness in the welded zone and in the HAZ in comparison to the basic metal.

## 4. Discussion

Microstructures significantly influence the mechanical properties and performance of alloys, particularly in Ti ($\alpha$, $\beta$)-composed alloys. Equiaxed microstructures, for instance, enhance fatigue strength and ductility, exhibiting favorable plastic deformation behavior. On the other hand, lamellar microstructures demonstrate high fracture toughness and exceptional resistance to creep and fatigue crack growth [10]. The microstructure resulting from various manufacturing processes heavily relies on stable and metastable phase transformations induced by thermo-mechanical processing.

Welding Titanium alloys involves local melting and rapid solidification under thermal stresses, where the coefficient of thermal expansion between 20 and 200˚C is 9.5 × 10 m/m˚C and we assume that it has some influence on the new phase formation. Phase formation during welding is dictated by the thermodynamic preferences of the alloyed elements, posing a challenge that has been the subject of recent simulations and calculations [10].

This study focuses on a joint of two plates with differing cross-sectional areas, influencing heat transfer during welding. This variance affects the cooling rate and the phases formed during the cooling process as can be shown in the simulation presented in **Figure 4**. Ti-6246 alloy is sensitive to stresses during thermomechanical processes, leading to the formation of different phases based on the combination of thermal stresses, thermodynamic aspects in the phase diagram, and the kinetics of phase formation.

Differences in heat flow from the central line of the welding reveal directional grain orientation as result. On the left side of the centerline in **Figure 2(d)** and equivalent zones in **Figure 4**, where heat flow is higher due to the plate's metal conductivity, an aspect ratio of approximately 0.2 is observed in grown grains in the left side of the metallography. Conversely, on the lower right side (**Figure 2(d)** and the equivalent zone in the calculation in **Figure 4**), where heat flow is primarily through convection in the first run of the welding process, equiaxed grains are obtained. **Figure 3(a)** in the bottom right side illustrates the development of acicular $\alpha$ coarsening and primary $\alpha$ grain marked by arrows, along with precipitates or inclusions of carbides, assumed to be stochiometric $Ti_2AlC$ formed by the 0.04 weight percent of carbon, as presented in **Table 1**.

The balance in welding energy, accounting for keyhole shape variation, was previously estimated based on wall temperature and keyhole depth [11]. Isothermal transformation of β-to-$\alpha$ occurred at various temperatures, with 600˚C identified as the most effective for a rich $\alpha$ phase [12] [13]. The rapid cooling of the welding spot, reaching room temperature within 3 minutes, was evident in the first run (**Figure 3(a)**), where no lamellar phases were detected. Subsequent runs (**Figure 3(b)**) exhibited nearly equal conductivity post-initial jointing, ensuring consistent heat transfer. **Figure 3(b)** presents the second run of the welding, where conductivity was nearly equal after the initial full jointing connection of the two plates, ensuring continuity in the heat transfer flow. **Figure 5** and **Figure 6** with the values in **Table 2** and **Table 3**, respectively, show different values of Vickers's hardness that fluctuate between 398 to 425 VDPHN (Vickers Diamond Pyramid Hardness Number) in the first welding run in the HAZ and the fused zone. The hardness obtained in the second welding run presents higher hardness in the HAZ and decreases to the center line of the fused zone, from 451 VDPHN to 423 VDPHN with similar fluctuations as in the first welding run.

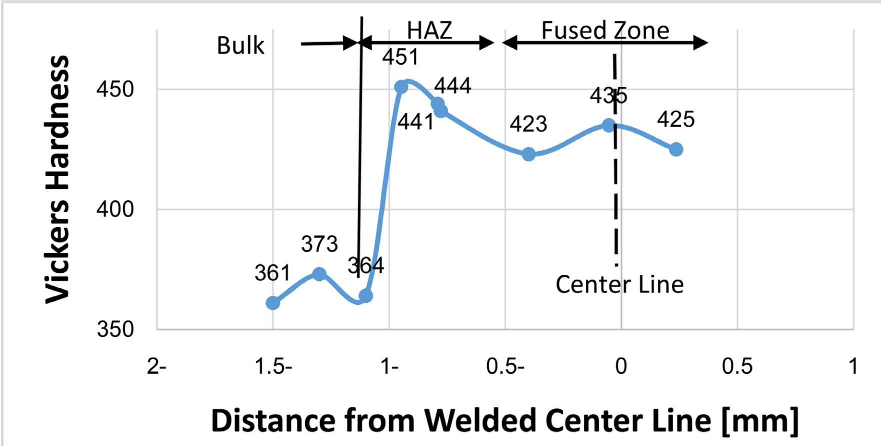


**Figure 6.** Vickers Hardness in the Fused Zone of the first EBW Run and the respective distance from the center line of the welded zone in a plot and in **Table 3** carried out along the lower line and arrows shown in **Figure 1(c)**.

**Table 3.** Vickers hardness in the fused zone of the first EBW run.

| Zone | Vickers Hardness | Distance from Center Line [μm] |
|---|---|---|
| | 361 | −1500 |
| Metal Bulk | 373 | −1300 |
| | 364 | −1100 |
| | 451 | −947.54 |
| Left HAZ | 444 | −790.35 |
| | 441 | −777.59 |
| | 423 | −398.73 |
| Fused Metal | 435 | −53.76 |
| | 425 | 236.15 |
| | 419 | 897.82 |
| Right Haz | 436 | 1064.61 |
| | 447 | 1896.01 |

Comparable hardness values were reported elsewhere for this alloy [7]. Electron microscopy and x-ray diffraction to examinate the increasing of the hardening of the fused zone and HAZ was carried out elsewhere and reveal a metastable soft orthorhombic martensite phase ($\alpha''$) formed in the very beginning of the $\beta$ to $\alpha$ transformation at high cooling rate in the Ti6-2-4-6 [14]. It's suggested that the $\alpha''$ phase itself might not be the primary reason for the increase in hardness. Instead, it's proposed that there's a rapid transformation of the orthorhombic phase to $\alpha'$ martensite due to the precipitation of the starter $\beta$ phase formed at high temperatures. This transformation is considered a mechanism for hardening. SEM micrographs reveal the $\beta$ phase structure and the initial formation of very fine $\alpha'$ martensite, indicating the early stages of transformation (**Figure 7(a)**).

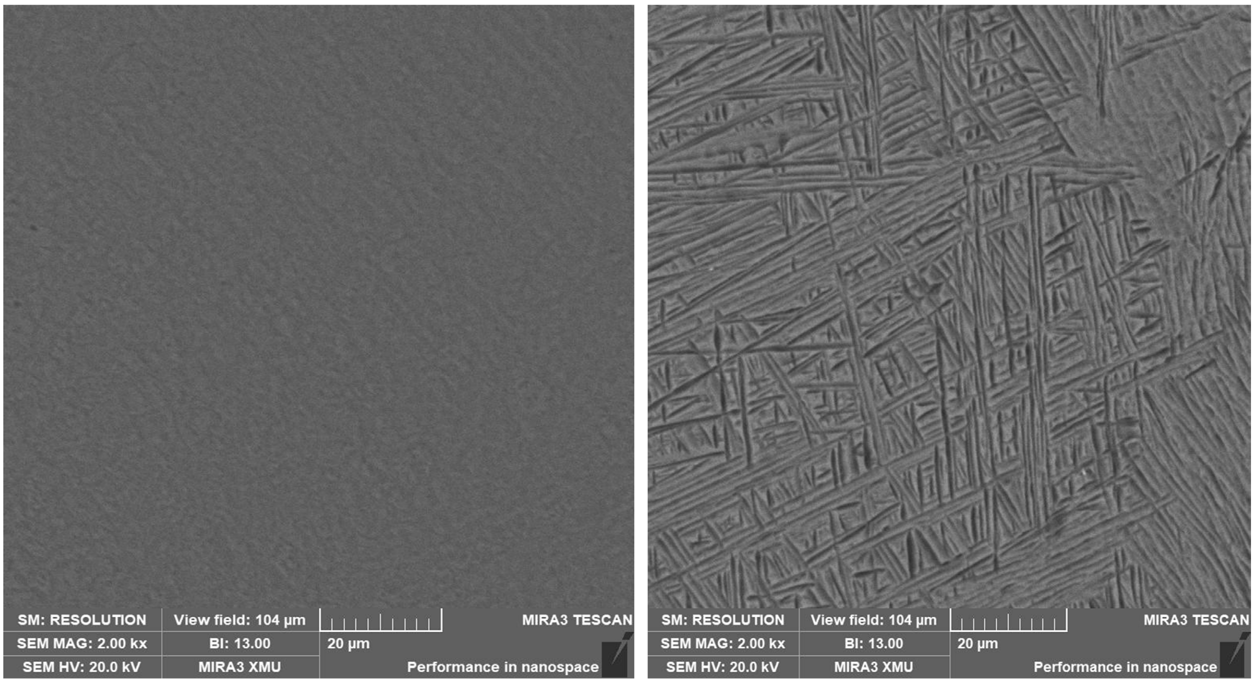


(a) (b)

**Figure 7.** SEM images at high magnification of (a) left-up corner area in **Figure 2(e)**, and (b) right down corner area of **Figure 2(b)**, presenting the changes in the microstructure of the fused zone and the as received alloy. **Figure 7(a)** shows the pre-saturated $\alpha'$ in $\beta$, and **Figure 7(b)** a saturate (black) $\alpha$ phase in $\beta$.

**Figure 7(b)** shows fully formed $\alpha$ martensite in the original state of the alloy before welding. It's suggested that the formation of the $\alpha'$ phase and the coherence between the BCC $\beta$ phase obtained at high temperatures and the hexagonal $\alpha'$ phase formed during rapid cooling of the fused zone contribute to the increase in hardness. The mutual habit planes between the $\alpha$ (HCP) and $\beta$ (BCC) phases are important, particularly in the early stages of $\alpha'$ phase formation. The coherency between the BCC $\beta$ phase obtained at high temperatures above 935˚C and the hexagonal $\alpha'$ phase formed during fast cooling is crucial for hardness increase. This coherency occurs in mutual habit planes, particularly $(0001)\alpha$ // $\{101\}\beta$ [15]. This coherency is available in the earliest stages of the $\alpha'$ phase formation and we assume that this is the fine microstructure obtained in **Figure 6(a)**. Martensite $\alpha$ formed in the as-received alloy after thermomechanical treatments increases the amount of $\alpha'$ phase in the $\beta$ phase up to a saturated state. This process leads to semi-coherent and incoherent habit planes, reducing hardness. In summary, the analysis suggests that the rapid transformation from the metastable orthorhombic phase to $\alpha'$ martensite, along with the coherency between phases, contributes to the increase in hardness in the titanium alloy. However, thermomechanical treatments can alter this effect by affecting the amount and coherency of the phases, ultimately impacting hardness.

## 5. Conclusions

This case study highlights the microstructure obtained post-welding. In summary, the conclusions are as follows:

1) The hardness of both the fused zone and the Heat Affected Zone (HAZ) exhibited an increase of nearly 20%.

2) We attribute this hardness increment to the coherency between $(0001)\alpha//\{101\}\beta$ planes of the BCC and HCP lattice, respectively.

3) The alteration in the grain grow microstructure is linked to the rapid cooling of the fused zone and HAZ, facilitated by the thermal mass of the plates as sported by simulation.

4) Variances in heat flow from the welding central line, attributed to differences in cross-sectional areas of the welded plates, resulted in directional grain orientation. Higher heat flow areas demonstrated a directional grain structure due to superior plate metal conductivity, while lower heat flow areas yielded equiaxed grains.

5) A noticeable aspect ratio of approximately 0.2 is observed in the grains with directional growth.

## Acknowledgements

The authors thank Mr. J. Sher for the EBW process and Dr. J. Rodnizki for the simulation.

## Conflicts of Interest

The authors declare no conflicts of interest regarding the publication of this paper.

## References

[1] Inakagi, I., Takechi, T., Shirai, Y. and Ariyasu, N. (2014) Application and Features of Titanium for the Aerospace Industry. Nippon Steel & Sumitomo Metal Technology Report No. 106 July 2014, UDC 669. 295: 629. 735. 3, 22-27. https://www.nipponsteel.com/en/tech/report/nssmc/pdf/106-05.pdf

[2] Williams, J.C. and Boyer, R. (2020) Opportunities and Issues in the Application of Titanium Alloys for Aerospace Components. *Metals*, **10**, 705. https://doi.org/10.3390/met10060705

[3] Filice, L., Gagliardi, F., Lazzaro, S. and Rocco, C. (2010) FE Simulation and Experimental Considerations on Titanium Alloy Superplastic Forming for Aerospace Applications. *International Journal of Material Forming*, **3**, 41-46. https://link.springer.com/article/10.1007/s12289-009-0415-y https://doi.org/10.1007/s12289-009-0415-y

[4] Fang, Y.-J., Jiang, X.-S., Mo, D.-F., Song, T.-F., Shao, Z.-Y., Zhu, D.-G., Zhu, M.-H. and Luo, Z.-P. (2018) Microstructure and Mechanical Properties of Electron Beam-Welded Joints of Titanium TC4 (Ti-6Al-4V) and Kovar (Fe-29Ni-17Co) Alloys with Cu/Nb Multi-Interlayer. *Advances in Materials Science and Engineering*, **2018**, Article ID 2042871. https://doi.org/10.1155/2018/2042871

[5] Alluaibi, M.H.I., Cojocaru, E.M., Rusea, A., Serban, N., Coman, G. and Cojocaru, V.D. (2020) Microstructure and Mechanical Properties Evolution during Solution and Ageing Treatment for a Hot Deformed, Above $\beta$-Transus, Ti-6246 Alloy. *Met-*

*als*, **10**, 1114. https://doi.org/10.3390/met10091114

[6] Alluaibi, M.H., Alturaihi, S.S., Cojocaru, E.M. and Cinca, I. (2019) Microstructural Evaluation During Thermomechanical Processing of Ti-6246 Titanium Alloy. *UPB Scientific Bulletin*, *Series B*: *Chemistry and Materials Science*, **81**, 225-234. https://www.researchgate.net/publication/331409347

[7] Huang, J. (2011) The Characterization and Modelling of Porosity Formation in Electron Beam Welded Titanium Alloys. Doctor Dissertation, The University of Birmingham. https://etheses.bham.ac.uk/id/eprint/3276/1/Huang_12_PhD.pdf

[8] Mendez, P.F. (2023) Calculation of Thermal Features in Welding and Additive Manufacturing. *IOP Conference Series*: *Materials Science and Engineering*, **1281**, 012021. https://iopscience.iop.org/article/10.1088/1757-899X/1281/1/012021/pdf https://doi.org/10.1088/1757-899X/1281/1/012021

[9] Burtscher, M., Weißensteiner, I., Wartbichler, R., Kirchheimer, K., Bernhard, C., Kiener, D. and Clemens, H. (2023) Precipitation Behavior of Hexagonal Carbides in a C Containing Intermetallic $\gamma$-Tial Based Alloy. *Journal of Alloys and Compounds*, **969**, Article ID 172400. https://doi.org/10.1016/j.jallcom.2023.172400

[10] Zhang, J.H., Li, X.X., Xu, D.S. and Yang, R. (2019) Recent Progress in the Simulation of Microstructure Evolution in Titanium Alloys. *Progress in Natural Science*: *Materials International*, **29**, 295-304. https://doi.org/10.1016/j.pnsc.2019.05.006

[11] Rai, R., Burgardt, P., Milewski, J.O., Lienert, T.J. and DebRoy, T. (2009) Heat Transfer and Fluid Flow during Electron Beam Welding of 21Cr-6Ni-9Mn Steel and Ti-6Al-4V Alloy. *Journal of Physics D*: *Applied Physics*, **42**, 025503. https://doi.org/10.1088/0022-3727/42/2/025503

[12] Pederson, R. (2004) The Microstructures of Ti-6A1-4V and Ti-6Al-2Sn-4Zr-6Mo and Their Relationship to Processing and Properties. Doctoral Thesis, Luleå University of Technology. https://www.diva-portal.org/smash/get/diva2:991452/FULLTEXT01.pdf

[13] Pederson, R., Niklasson, F., Skystedt, F. and Warren, R. (2012) Microstructure and Mechanical Properties of Friction- and Electron Beam Welded Ti-6Al-4V and Ti-6Al-2Sn-4Zr-6Mo. *Materials Science and Engineering A*, **552**, 555-565. https://doi.org/10.1016/j.msea.2012.05.087

[14] Greenfield, M.A. and Duvall, D.S. (1975) Welding of an Advanced High Strength Titanium Alloy. *Welding Research Supplement*, 73-80. https://app.aws.org/wj/supplement/WJ_1975_03_s73.pdf

[15] Britton, T.B., Dunne, F.P.E. and Wilkinson, A.J. (2015) On the Mechanistic Basis of Deformation at the Microscale in Hexagonal Close-Packed Metals. *Proceedings of the Royal Society A*: *Mathematical*, *Physical and Engineering Sciences*, **471**, 20140881-20140881. https://doi.org/10.1098/rspa.2014.0881 http://rspa.royalsocietypublishing.org/content/471/2178/20140881